Optimizing the Ag/Bi ratio for controlled growth of $AgBiS_2$ thin films via a two-stage process

U. CHALAPATHI[1], KIRAKALA KIRAN KUMAR[2], ATHIPALLI DIVYA[3], RADHALAYAM DHANALAKSHMI[4], KRITHIKAA MOHANARANGAM[5], CUDDAPAH DHANANJAYA RAO[6], SAMBASIVAM SANGARAJU[7], C. SAFAROV ABDUVAHID SHUKUROVICH[8], VASUDEVAREDDY MINNAM REDDY[9,10], SI-HYUN PARK[1,*]
[1]*Department of Electronic Engineering, Yeungnam University, 280 Daehak-Ro, Gyeongsan, Gyeongbuk 38541, South Korea*
[2]*Department of General Physics, Termez State University, Termez, 190111, Uzbekistan*
[3]*Department of Physics, School of Technology, The Apollo University, Chittoor, A.P., 517127, India*
[4]*Department of Physics, University of Santiago of Chile (USACH), Santiago, Chile*
[5]*Symbiosis Institute of Technology, Pune Campus, Symbiosis International (Deemed University), Pune, India*
[6]*Department of Physics and Astronomy, Navoi State University, Navoi, 210100, Uzbekistan*
[7]*National Water & Energy Center, United Arab Emirates University, Al Ain, 15551, UA*
[8]*Department of Physics and Mathematics Termez State University, Termez, 190111, Uzbekistan*
[9]*Department of Mathematics, Saveetha School of Engineering, Saveetha Institute of Medical and Technical Sciences (SIMATS), Thandalam, Chennai, 602105, India*
[10]*School of Chemical Engineering, Yeungnam University, Gyeongsan-si, 38541, South Korea*

This study focuses on synthesizing $AgBiS_2$ thin films by sulfurizing Bi/Ag metal precursors in a graphite box. At a ratio of 1.26, Ag_2S secondary phase was present, resulting in nonuniform grain growth, a 0.99 eV energy gap, and 640 Ω cm resistivity. Near-stoichiometric ratios (1.07 and 0.90) eliminated secondary phases, yielding phase-pure $AgBiS_2$ with uniform grains, a 1.02 eV energy gap, and 13.7 Ω cm resistivity. At a 0.79 ratio, increased crystallinity and resistivity (25 Ω cm) were observed. These results highlight the importance of stoichiometry in fabricating high-quality $AgBiS_2$ films for solar cells.

(Received May 8, 2025; accepted December 4, 2025)

Keywords: $AgBiS_2$, Thin films, Evaporation

1. Introduction

The quest for light harvesters that are both abundant on Earth and non-toxic is paramount for advancing photovoltaic technology. In recent years, considerable attention has been directed towards ternary chalcogenides within the Cu and Ag-based compound families due to their plentiful presence and environmentally friendly characteristics. Among these, silver bismuth sulfide ($AgBiS_2$), a member of the I-III-VI family, stands out as a promising contender for its applications in photovoltaics, photoelectrochemical systems, thermoelectric, and supercapacitors. This is primarily due to its favorable optoelectronic properties [1–6]. $AgBiS_2$ boasts a direct optical bandgap of 0.8 eV and a high absorption coefficient (10^5 cm^{-1}), rendering it well-suited for employment in solar cells. The $AgBiS_2$-based solar cells demonstrated a power conversion efficiency of 10% [7, 8]. However, the $AgBiS_2$-based solar cells described in literature were fabricated utilizing $AgBiS_2$ quantum dots, a process that involved intricate and time-consuming procedures [9-14]. Furthermore, solutions containing $AgBiS_2$ quantum dots are susceptible to instability and may aggregate over time. Additionally, the presence of defects induced by organic ligands impose limitations on the reproducibility of the devices, necessitating ligand exchange and surface engineering of the prepared quantum dots. Challenges such as ensuring batch-to-batch stability of the final composition and implementing effective passivation techniques are common in nanoparticle synthesis approaches [1]. Attaining uniformly dispersed particles in a specific solvent to establish stable ink for thin film deposition presents further obstacles.

Numerous investigations have documented the production of $AgBiS_2$ thin films through various solution methods such as chemical bath deposition (CBD) [15–17], successive ionic layer adsorption and reaction (SILAR) [18, 19], spray pyrolysis [20], and spin coating [21–23]. Rodriguez et al. [15] pioneered the synthesis of photoconductive $AgBiS_2$ thin films with a direct bandgap of 0.96 eV, achieved by heating Bi_2S_3/Ag_2S layers grown via CBD at 300 ^oC under a nitrogen atmosphere of 100 mTorr. Subsequently, Nesheva et al. [16] and Yao et al. [17] employed the same CBD method, with Nesheva studying the photoelectrical properties and Yao investigating photodetection capabilities, particularly for X-ray detection. Huang et al. [18] utilized a two-stage SILAR technique to synthesize $AgBiS_2$ nanocrystalline thin films, subsequently developing liquid-junction semiconductor-sensitized solar cells with modest power conversion efficiency (PCE) of 0.76%. Calva-Yanez et al. [19] similarly utilized the two-stage SILAR method, achieving a

higher PCE of 2.87% in inorganic-organic hybrid solar cells by depositing $AgBiS_2$ films on TiO_2 coated substrates. Pai et al. [20] deposited $AgBiS_2$ thin films via spray pyrolysis, leading to planar heterojunction solar cells with a PCE of 1.5%. Gu et al. [21] employed spin coating to synthesize nanocrystalline cubic $AgBiS_2$ thin films, revealing both indirect and direct bandgaps of 0.87 eV and 1.21 eV, respectively. Oh et al. [22] reported the synthesis of water-resistant $AgBiS_2$ nanocrystalline thin films via spin coating, achieving notable solar cell efficiency of 5.75%. Lastly, Kelley et al. [23] demonstrated the synthesis of photoconductive $AgBiS_2$ quantum dot thin films through spin coating $AgBiS_2$ quantum dot inks.

The availability of $AgBiS_2$ thin films synthesized via physical vapor deposition (PVD) methods is limited. Gao et al. [24] demonstrated the fabrication of such films through magnetron sputtering, resulting in grain sizes of 1.2 μm and a bandgap of 0.853 eV. There- fore, the utilization of PVD techniques for $AgBiS_2$ thin film fabrication is crucial due to the controllability of growth conditions and environmentally friendly synthesis. Additionally, PVD-produced films exhibit desirable properties such as adhesion, resistance, and durability, making them suitable for photovoltaic applications. In our recent work, we synthesized $AgBiS_2$ thin films by sulfurizing thermally evaporated Bi/Ag metal stacks, exploring the impact of sulfurization temperature on film growth [25]. The elemental composition significantly influences ternary compound formation, as observed in $CuSbS_2$ and $AgSbS_2$ thin films where deviations from stoichiometric composition led to secondary phase formation [26, 27]. Hence, precise control over composition ratios during growth is imperative for these compounds. Consequently, our study investigates the influence of the Ag/Bi ratio on the physicochemical properties of $AgBiS_2$ films prepared via a two-stage method. We examine the structural, microstructural, optical, and electrical characteristics of the $AgBiS_2$ films concerning the Ag/Bi ratio.

2. Experimental details

2.1. Evaporation of the Bi/Ag metal stacks

Deposition of the Bi/Ag metal stack was conducted using a two-source vacuum evaporation unit. Prior to deposition, soda-lime glass substrates were meticulously cleaned chemically and ultrasonically, along with loading Ag and Bi metal slugs into the chamber. Evaporation utilized foil trough tungsten (W), maintaining a constant boat-to-substrate distance of 36 cm. The chamber's base pressure was sustained at 2×10^{-6} Torr. Thickness estimates for Bi and Ag, crucial for forming a 1 μm $AgBiS_2$ film via solid-state reaction in an S atmosphere, were deduced from mass density calculations as 400 nm and 190 nm, respectively. Consequently, Bi thickness varied from 380 to 440 nm in 20 nm increments while maintaining Ag thickness at 190 nm. This allowed exploration of the Ag/Bi ratio's impact on $AgBiS_2$ film growth. Evaporation rates for Bi and Ag were held constant at 4 $\mathring{A}$ / s using a quartz crystal thickness monitor. All depositions were conducted at room temperature.

2.2. Transformation of Bi/Ag stacks into $AgBiS_2$

The evaporated Bi/Ag precursors were subjected to chalcogenization at 400^{o}C for 30 min to transform them into $AgBiS_2$. The sulfurization temperature and duration were selected based on our previous study [25], which identified 400°C and 30 min as the optimal conditions for preparing high-quality $AgBiS_2$ thin films. Elemental S was used as the sulfur source. The quartz tube was pressurized with nitrogen up to atmospheric pressure to elevate sulfur pressure and mitigate material re-evaporation. The temperature of the furnace was ramped up at a rate of 10^{o}C/min and the sulfurization ensued for 30 minutes at 400^{o}C, followed by cooling to 250^{o}C at a rate of 2^{o}C/min, and subsequently allowed to cool naturally.

2.3. Characterizations

A PANalytical XRD, utilizing a Cu Kα source (0.15406 nm), operated in grazing incidence mode (ω = 3^o), was employed to ascertain the crystal structure and phase-purity of the samples. Surface morphologies of the films were documented using a Hitachi S-4800 FESEM, while elemental composition was determined via EDS analysis. Spectral transmittance in the range of 300–2500 nm was recorded using a Cary 5000 UV-Vis-NIR double-beam spectrophotometer. Lastly, electrical properties of the films were determined using an ECOPIA Hall measurement system (HMS-3000, VER 3.53).

3. Results and discussion

3.1. Compositional analysis

Table 1 presents composition data for $AgBiS_2$ films with varying Bi thicknesses, revealing systematic shifts in Ag and Bi concentrations as the Bi layer thickness increases. The elemental composition of $AgBiS_2$ consists of 25% Ag, 25% Bi, and 50% S. For example, the film crafted with a Bi layer thickness of 380 nm exhibited an Ag-rich, Bi-poor composition, with Ag/Bi and S/(Ag+Bi) ratios of 1.26 and 1.0, respectively. Increasing the Bi thickness from 400 nm to 420 nm resulted in higher Bi content and lower Ag content, with the Ag/Bi ratio varying from 1.07 to 0.90. Further increasing the Bi thickness to 440 nm reduced the Ag/Bi ratio to 0.79 without altering the S/(Ag+Bi) ratio. Consequently, increasing the Bi layer thickness decreased the Ag/Bi ratio from 1.26 to 0.79. Fig. 1 displays the EDS spectra of $AgBiS_2$ films fabricated by varying the Ag/Bi ratio from 1.26 to 0.79, revealing peaks corresponding to Ag, Bi, and S under all conditions. It is evident that increasing the composition ratio enhances the Ag peak intensity while decreasing the Bi intensity, consistent with the atomic percentages outlined in Table 1.

Table 1. EDS data of $AgBiS_2$ films produced from the Bi/Ag stacks with different thicknesses

Bi/Ag stack		Atomic percentage		Ratio	
thickness (nm)	Ag	Bi	S	Ag/Bi	S/(Ag+Bi)
380/190	27.8	22.1	50.1	1.26	1.00
400/190	26.4	24.7	48.9	1.07	0.96
420/190	25.1	27.5	47.4	0.90	0.90
440/190	23.2	29.5	47.3	0.79	0.90

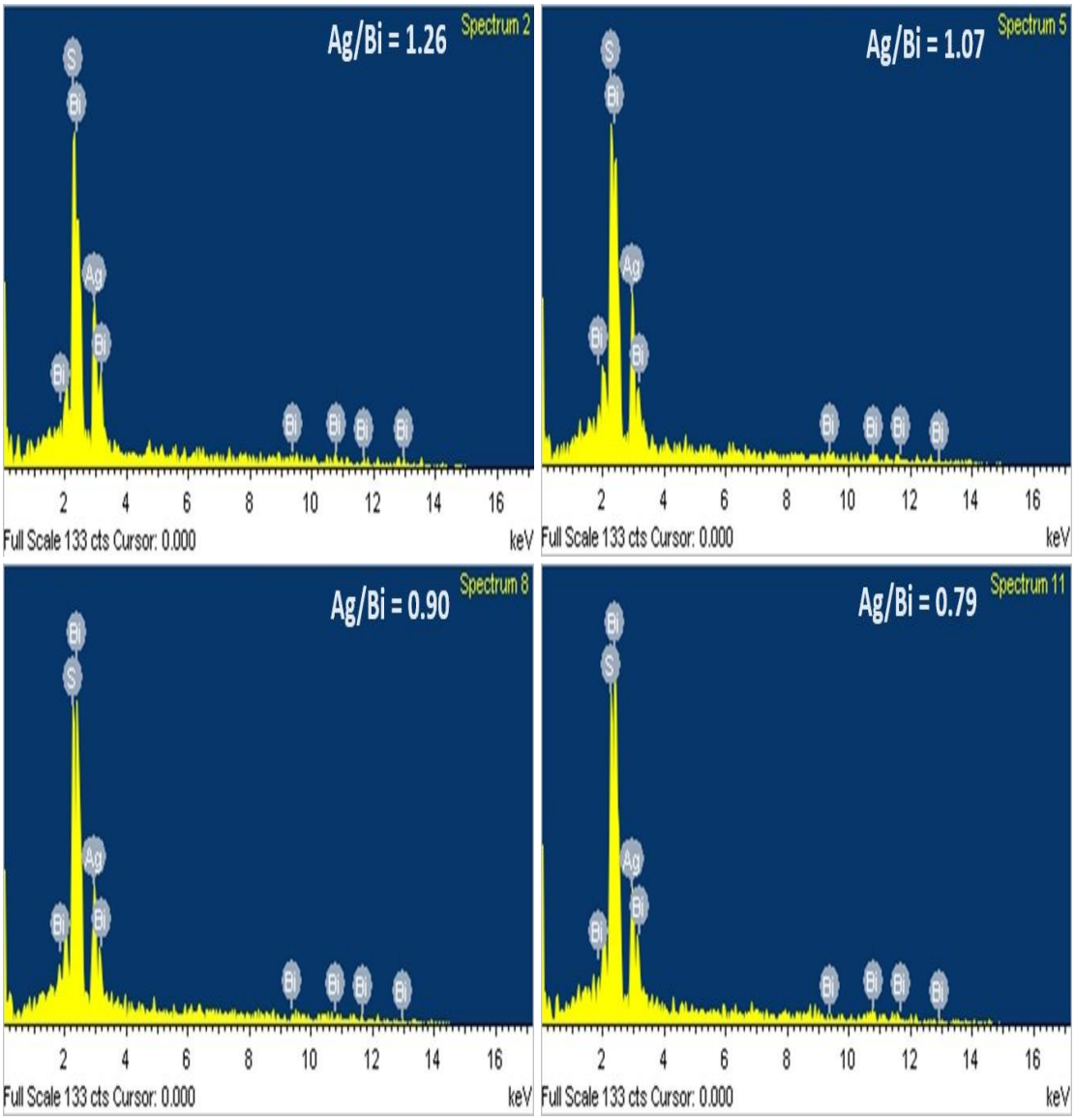

Fig. 1. EDS spectra of the $AgBiS_2$ films produced from Bi/Ag stacks with varying thicknesses of Bi (colour online)

3.2. Structural analysis

Fig. 2 illustrates the XRD patterns of $AgBiS_2$ films fabricated with various Ag/Bi ratios. When the Ag/Bi ratio is 1.26, the film exhibits predominant diffraction peaks at 27.28^o, 31.54^o, 45.27^o, 53.66^o, and 56.30^o, matching the standard diffraction pattern of $AgBiS_2$ (JCPDS Card No. 01-089-2045). Additionally, weak peaks at 34.40^o, 36.88^o, and 37.72^o correspond to monoclinic Ag_2S (JCPDS Card No. 014-0072). The dominant peaks of $AgBiS_2$ indicate formation of this phase in cubic crystal structure with (111) preferred orientation and lattice parameter of 0.566 nm. Reducing the Ag/Bi ratio to 0.90 eliminates the diffraction peaks of Ag_2S, indicating phase-pure $AgBiS_2$. Further reduction to 0.79 does not significantly affect peak positions/intensities, with only cubic $AgBiS_2$ peaks present. Secondary phases like Bi_2S_3 do not appear at this

composition, underscoring the importance of near-stoichiometric composition for phase-pure film growth. A slight shift in the intense (111) peak and a reduction in FWHM suggest variations in lattice parameter and crystallite size, ranging from 0.5664 to 0.5660 nm and from 18.4 to 23 nm, respectively, as the composition shifts from 1.26 to 0.79 [28].

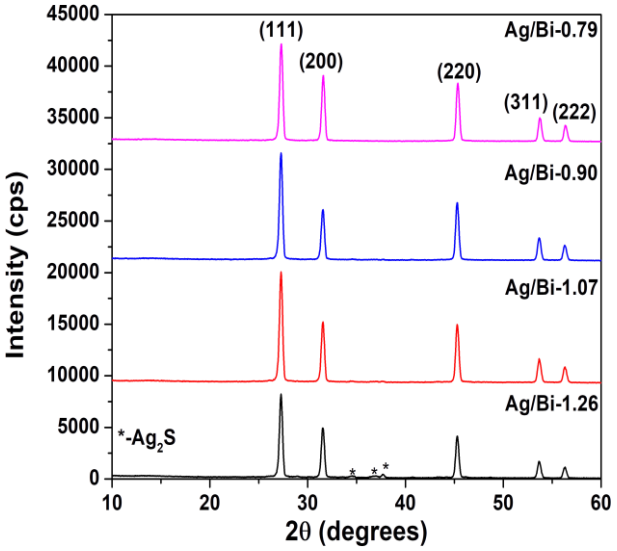

Fig. 2. XRD patterns of $AgBiS_2$ films fabricated with different Ag/Bi ratios (colour online)

The phase purity of the samples was further examined using Raman spectroscopy, as presented in Fig. 3.

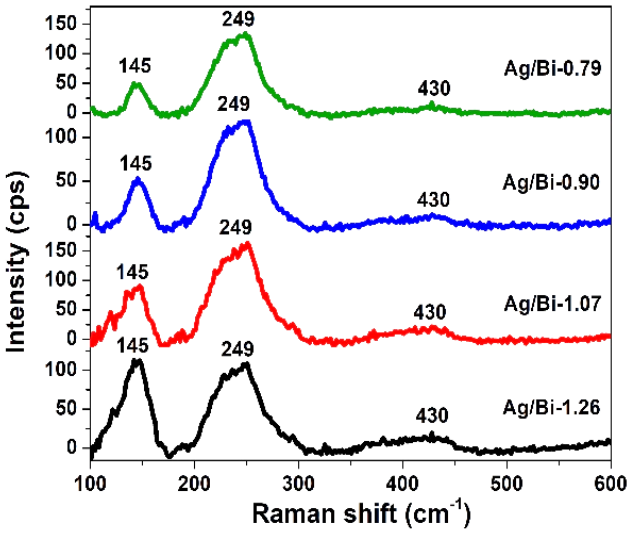

Fig. 3. Raman spectra of $AgBiS_2$ films fabricated with different Ag/Bi ratios (colour online)

The $AgBiS_2$ films synthesized with varying Ag/Bi ratios displayed Raman features at 145 cm^{-1}, 249 cm^{-1}, and 430 cm^{-1}. Notably, the intensity of the 145 cm^{-1} mode decreased, whereas the 249 cm^{-1} mode became more prominent as the Ag/Bi ratio was reduced from 1.26 to 0.79, reflecting changes in the local chemical environment. These observed modes are consistent with the reported Raman bands of $AgBiS_2$ at 147 cm^{-1}, 237–248 cm^{-1}, and 436 cm^{-1} [29, 30]. Furthermore, the absence of Raman signatures corresponding to Bi_2S_3 [31] and Ag_2S [32] suggests that these secondary phases are either not present or lie below the probing depth of the Raman measurement.

3.3. Morphological analysis

Fig. 4 displays the microstructure of $AgBiS_2$ films fabricated with varying Ag/Bi ratios. The micrographs illustrate that the grain growth of $AgBiS_2$ is notably influenced by these ratios. For instance, the $AgBiS_2$ film fabricated with the composition ratio of 1.26 reveals distinct nonuniform grains measuring 1.0–2.0 μm in size, along with crater-like regions on the surfaces. This nonuniform grain growth is likely due to the Ag_2S and $AgBiS_2$ phases, as confirmed by XRD analysis. Conversely, when the composition ratio varied from 1.07 to 0.90, a significant improvement in compactness, grain size, and uniformity, with an average grain size of 2.0–2.5 μm were observed. This enhancement in grain growth and morphology correlates with an increasing Ag/Bi ratio, suggesting improved phase purity of the films as observed from XRD analysis. Further reduction of the Ag/Bi ratio to 0.79 results in decreased grain size (1.0–2.0 μm) and the formation of crater-like regions on the surface, indicating a loss of material with higher Bi concentration. These observations underscore the importance of a near-stoichiometric composition for achieving compact and large-grained $AgBiS_2$ thin films.

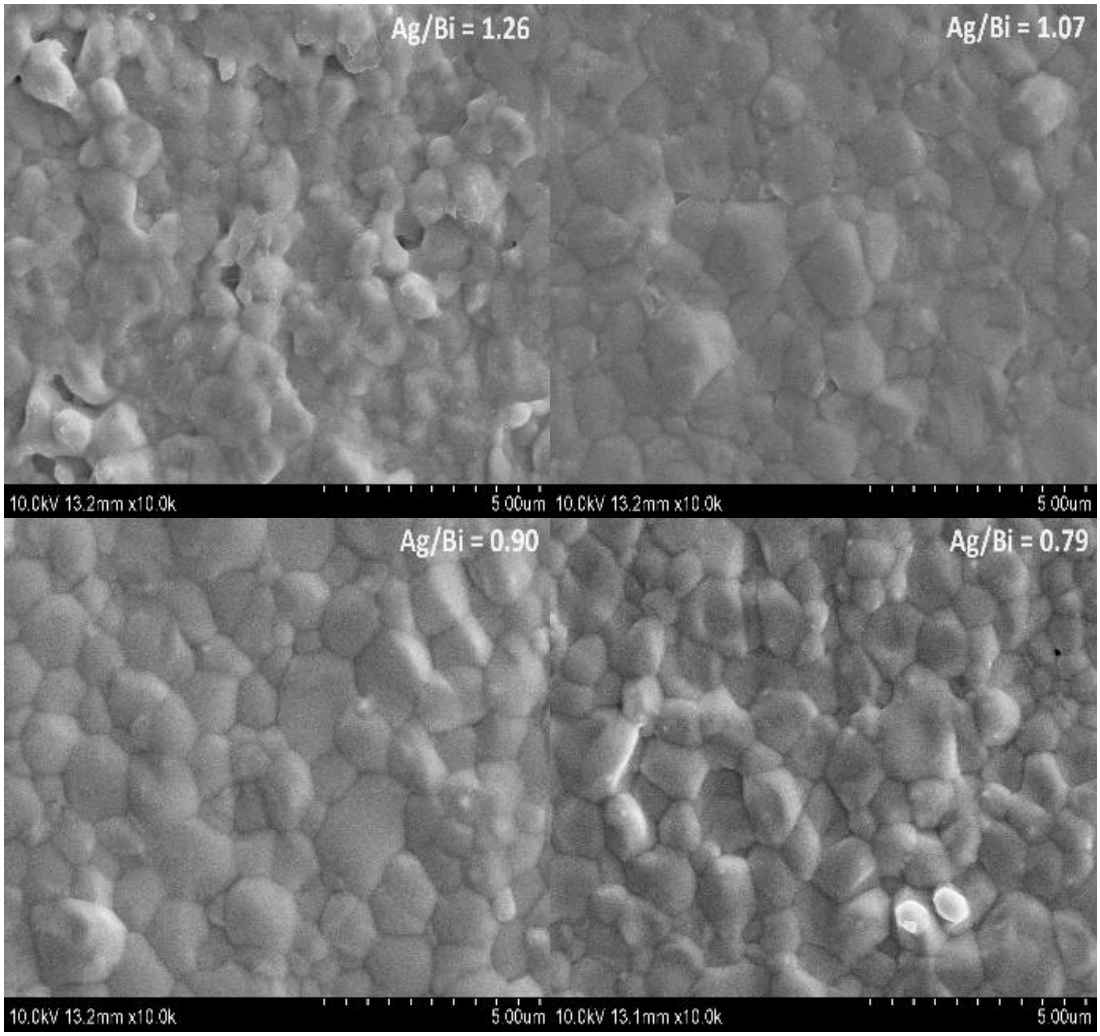

Fig. 4. FESEM micrographs of the $AgBiS_2$ films fabricated with different Ag/Bi ratios

Fig. 5 depicts cross-sectional FESEM images of the films, illustrating the vertical grain growth as the Ag/Bi ratios vary. Notably, the composition ratios exert a significant influence on both film thickness and grain size throughout the thickness. For instance, at a composition ratio of 1.26, a compact and firmly adherent layer form with columnar grain growth up to 800 nm in thickness. Conversely, reducing the composition ratio from 1.07 to 0.90 results in increased grain size, reaching 1000 nm throughout the thickness. Further reduction to a composition ratio of 0.79 increases film thickness to 1200 nm, characterized by columnar grains covered by a smear top surface.

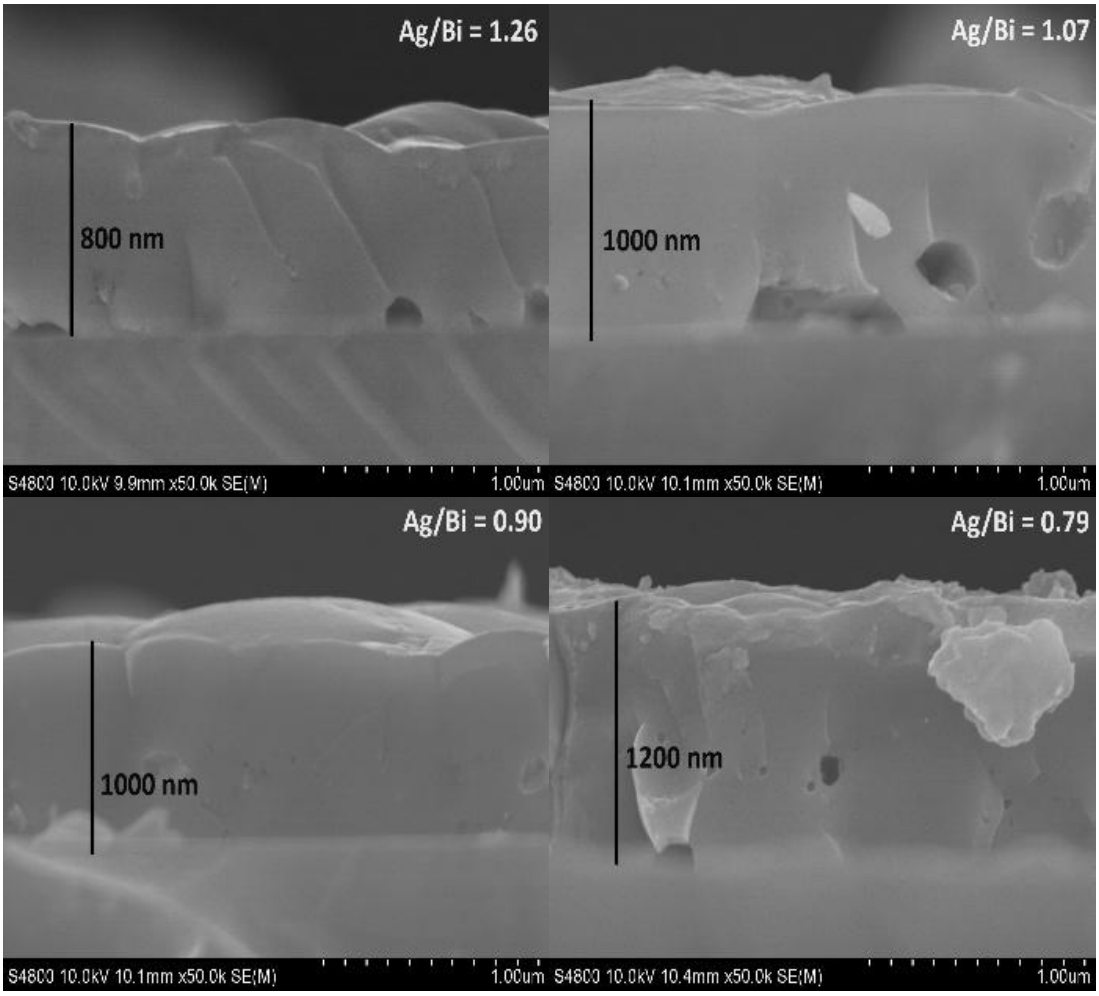

Fig. 5. Cross-sectional FESEM images of the $AgBiS_2$ films fabricated with different Ag/Bi ratios

3.4. Optical absorption

The optical properties of the $AgBiS_2$ films were determined using the transmittance data depicted in Figure 6. It's notable that varying the Ag/Bi ratio did not significantly alter the transmittance of the films. For instance, the film with the composition ratio of 1.26 exhibited a low optical transmittance (15%) at longer wavelengths and displayed an onset of absorption ranging from 1480 to 1130 nm. This onset of absorption aligns with the reported onset of absorption for $AgBiS_2$ [15, 24]. However, the transition corresponding to Ag_2S, a secondary phase in this film, was not discernible due to the strong absorption of the $AgBiS_2$ phase. Decreasing the composition ratio from 1.07 to 0.90 leads to a slight increase in transmittance to 18%, attributed to enhanced crystallinity and grain size observed from XRD and FESEM analyses. Further reduction in the Ag/Bi ratio to 0.79 marginally decreased transmittance to 15% due to the formation of crater-like regions on the film surface, as observed in FESEM images.

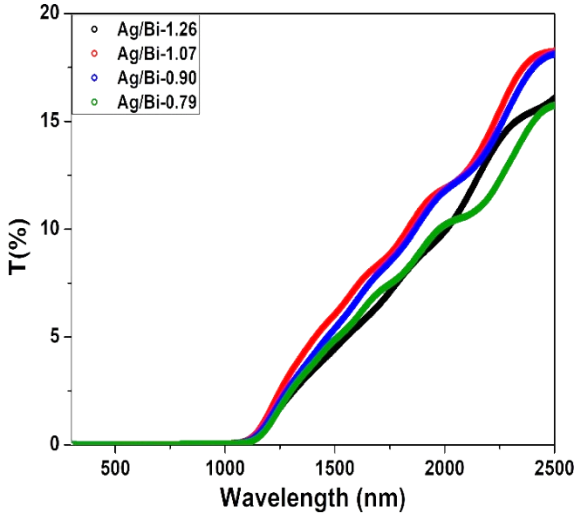

Fig. 6. Spectral transmittance curves of $AgBiS_2$ films fabricated with different Ag/Bi ratios (colour online)

Fig. 7 presents the $(\alpha h\nu)^2$ versus $h\nu$ curves of $AgBiS_2$ films fabricated with varying Ag/Bi ratios to ascertain their bandgap energies. The optical absorption coefficient was estimated using $\alpha_\lambda = \ln(1/T_\lambda)/t$, where t represents the film thickness [16, 33, 34]. The energy gap of the $AgBiS_2$ film

with the composition ratio of 1.26 was determined to be 0.99 eV, with an uncertainty of ±0.02 eV. Reducing the Ag/Bi ratio from 1.07 to 0.90 slightly increased the energy gap from 0.99 to 1.02 eV, while a further decrease to 0.79 led to a slight decrease in the energy gap to 0.99 eV. These energy gap values are close to the reported values of $AgBiS_2$ [15, 16]. The slightly lower energy gaps observed for $AgBiS_2$ films with the composition ratios of 1.26 and 0.79 are due to Ag-rich and Ag-poor compositions, respectively.

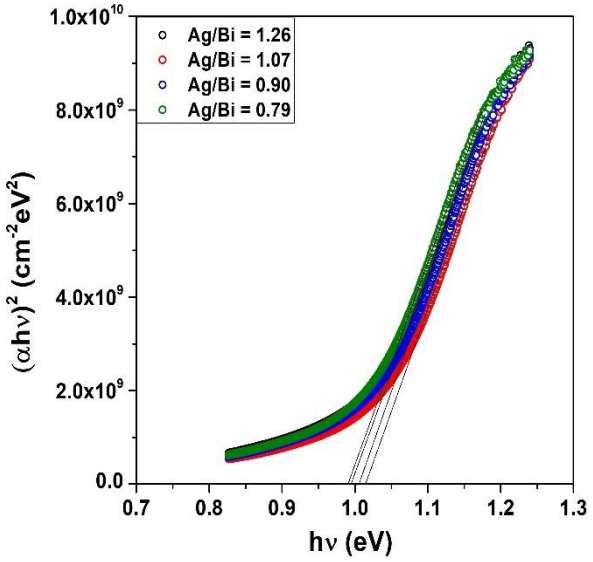

Fig. 7. $(ahv)^2$ vs. hv curves of $AgBiS_2$ films fabricated with different Ag/Bi ratios (colour online)

3.5. Electrical properties

Table 2 illustrates the electrical characteristics of $AgBiS_2$ films produced with varying Ag/Bi ratios. A negative Hall coefficient was observed in the film synthesized with the composition ratio of 1.26, indicative of its n-type behavior attributed to the presence of Ag_2S secondary phase. Conversely, films created with decreasing Ag/Bi ratios from 1.07 to 0.79 displayed a positive Hall coefficient, reflecting their p-type conductivity. In Table 2, the electrical resistivity of the film fabricated with an Ag/Bi ratio of 1.26 measured 640 Ω cm, whereas it decreased to 2.5 Ω cm at 1.07 and increased from 13.7 to 25 Ω cm with further reduction of the Ag/Bi ratio to 0.79. Rodriguez et al. [35] reported an electrical resistivity of $1.92x10^4$ Ω cm for the $AgBiS_2$ films prepared by CBD method. The obtained resistivity values are lower than the reported values. The higher resistivity in the Ag-rich (Ag/Bi = 1.26) film was attributed to its mixed-phase nature, while the increase in resistivity with decreasing Ag/Bi ratio from 1.07 to 0.79 may be attributed to higher Bi content. The hole mobility of the film fabricates with the composition ratio of 1.26 was 0.32 $cm^2V^{-1}s^{-1}$, while it increased from 9.7 to 21.0 $cm^2V^{-1}s^{-1}$ with a decrease to 0.90 and then reached 9.5 $cm^2V^{-1}s^{-1}$ at an Ag/Bi ratio of 0.79. Lower mobilities in both the Ag-rich (1.26) and Ag-poor (0.79) films were attributed to smaller grain sizes, while the higher hole mobility in near-stoichiometric films (1.07 and 0.90) was a result of compact, large-grained, and phase-pure films. Regarding carrier concentrations, the Ag-rich (1.26) film exhibited a concentration of $-6.2x10^{16}$ cm^{-3}, whereas near-stoichiometric films (1.07 and 0.90) ranged from $(2.50–2.2)\times10^{17}$ cm^{-3}, and the Ag-poor film (0.79) showed a decreased concentration of 1.5×10^{17} cm^{-3}. Yasaman [36] reported a hole mobility of 2.88 $cm^2V^{-1}s^{-1}$ and carrier concentration of $3.2x10^{14}$ cm^{-3} for the $AgBiS_2$ films prepared form the precursor method followed by spin coating. In comparison, the $AgBiS_2$ films prepared in this study with Ag/Bi ratios of 1.07–0.79 exhibit higher hole mobilities and carrier concentrations, indicating the superior quality of the films.

Table 2. Electrical properties of $AgBiS_2$ films fabricated with different Ag/Bi ratios

Ag/Bi ratio	Resistivity (Ω cm)	Mobility ($cm^2V^{-1}s^{-1}$)	Carrier conc. (cm^{-3})
1.26	640	0.32	$-6.2x10^{16}$
1.07	2.5	9.70	$2.5x10^{17}$
0.90	13.7	21.0	$2.2x10^{17}$
0.79	25	9.5	$1.2x10^{17}$

4. Conclusions

The process involved in fabricating $AgBiS_2$ thin films entailed sulfurizing Bi/Ag metal precursors deposited via thermal evaporation. The Bi layer thickness ranged from 380 to 440 nm, while the Ag layer remained fixed at 190 nm to investigate the impact of the Ag/Sb ratio on film growth and properties. Films fabricated with a composition ratio of 1.26 exhibited a secondary Ag_2S phase alongside the dominant cubic $AgBiS_2$ phase. Reducing the composition ratio from 1.07 to 0.79 led to the elimination of the Ag_2S phase, resulting in phase-pure $AgBiS_2$ films. Moreover, decreasing the composition ratio from 1.26 to 0.79 increased crystallite size from 18.4 to 23 nm. Improvements in compactness, uniformity, and grain size were observed in films with reduced Ag/Bi ratios, specifically from 1.26 to 0.90, although a further decrease to 0.79 diminished these characteristics. The energy gap of $AgBiS_2$ films ranged from 0.99 to 1.02 eV as the composition ratio varied from 1.26 to 0.79. Near-stoichiometric $AgBiS_2$ films (ratios of

1.07 and 0.90) displayed slightly lower electrical resistivity, higher hole mobilities, and carrier concentrations compared to Ag-rich (1.26) and Ag-poor (0.79) films. This study underscores the necessity of a near-stoichiometric composition for producing phase-pure, large-grained $AgBiS_2$ films possessing favorable optical and electrical properties conducive to solar cell applications.

Acknowledgements

This research was supported by the Gyeongsangbuk-do RISE (Regional Innovation System & Education) project.

References

[1] M. Bernechea, N. Cates, G. Xercavins, D. So, A. Stavrinadis, G. Konstantatos, Nature Photonics **10**, 521 (2016).
[2] L. Jiang, Y. Li, J. Peng, L. Cui, R. Li, Y. Xu, W. Li, Y. Li, X. Tian, Q. Lin, J. Mater. Chem. C **8**, 2436 (2020).
[3] D. Chen, S. B. Shivarudraiah, P. Geng, M. Ng, C.-H. A. Li, N. Tewari, X. Zou, K. S. Wong, L. Guo, J. E. Halpert, ACS Appl. Mater. Interf. **14**, 1634 (2021).
[4] S. Akhil, R. G. Balakrishna, J. Mater. Chem. A **10**, 8615 (2022).
[5] I. Burgues-Ceballos, Y. Wang, G. Konstantatos, Nanoscale **14**, 4987 (2022).
[6] Y. Wang, L. Peng, Z. Wang, G. Konstantatos, Adv. Energy Mater. **12**, 2200700 (2022).
[7] X. Li, H. Yu, X. Ma, Z. Liu, J. Huang, Y. Shen, M. Wang, Chem. Eng. J. **495**, 153328 (2024).
[8] J. Lee, C. Sun, J. Park, C. Kim, S. Lee, D. Lee, M.-H. Lee, B. Kim, Y. H. Kim, J. Kim, S. Lee, S. Jeong, W. B. Ying, X. Song, S. Cho, F. Rotermund, Y.-H. Kim, J.-Y. Lee, Adv. Mater. **37**, 2413081 (2025).
[9] J. Van Embden, A. S. Chesman, E. Della Gaspera, N. W. Duffy, S. E. Watkins, J. J. Jasieniak, J. Am. Chem. **136**, 5237 (2014).
[10] P. Wainer, O. Kendall, A. Lamb, S. J. Barrow, A. Tricoli, D. E. Gomez, J. van Embden, E. Della Gaspera, Chem. Mater. **31**, 9604 (2019).
[11] Aryan Mourya, Yongtao Qu, Kuldeep Singh Gour, J. Phys. Energy **7**, 042006 (2025).
[12] Zongwei Li, Huchen Han, Lingfeng Chao, Yonghua Chen, Gaojie Chen, Wei Huang, Electromagn. Sci. **3**, 0090451 (2025).
[13] Lin Yuan, Yang Li, Yang Liu, Kunyuan Lu, Guozheng Shi, Xiang Sun, Yong Li, Xinyu Dong, Yuran Xiao, Lizhen Huang, Zeke Liu, Wanli Ma, Angew. Chem. **137**, e202416369 (2025).
[14] Seungmin Baek, Young-Ho Lee, So Jeong Shin, Hyo-Geun Kwan, Jae Young Noh, Jong H. Kim, Sang-Wook Kim, Sunghoon Kim, Mater. Sci. Mater. Electron. **199**, 109812 (2025).
[15] A. N. Rodriguez, M. Nair, P. Nair, MRS Online Proc. Libr. **730**, 1 (2002).
[16] D. Nesheva, Z. Aneva, B. Pejova, I. Grozdanov, A. Petrova, J. Optoelectron. Adv. M. **11**(9), 1347 (2009).
[17] F. Yao, L. Jiang, Y. Qi, R. Li, Y. Li, Y. Xu, H. Liu, Q. Lin, Appl. Mater. Today **26**, 101262 (2022).
[18] P.-C. Huang, W.-C. Yang, M.-W. Lee, J. Phys. Chem. C **117**, 18308 (2013).
[19] J. Calva-Yanez, O. Perez-Valdovinos, E. Reynoso-Soto, G. Alvarado-Tenorio, O. Jaramillo-Quintero, M. Rincon, J. Phys. D: Appl. Phys. **52**, 125502 (2019).
[20] N. Pai, J. Lu, D. C. Senevirathna, A. S. Chesman, T. Gengenbach, M. Chatti, U. Bach, P. C. Andrews, L. Spiccia, Y.-B. Cheng, A. N. Simonov, J. Mater. Chem. C **6**, 2483 (2018).
[21] E. Gu, X. Lin, X. Tang, G. J. Matt, A. Osvet, Y. Hou, S. Jager, C. Xie, A. Karl, R. Hock, C. J. Brabec, J. Mater. Chem. C **6**, 7642 (2018).
[22] J. T. Oh, S. Y. Bae, S. R. Ha, H. Cho, S. J. Lim, D. W. Boukhvalov, Y. Kim, H. Choi, Nanoscale **11**, 9633 (2019).
[23] M. L. Kelley, F. Ahmed, S. L. Abiodun, M. Usman, M. U. Jewel, K. Hussain, H.-C. zur Loye, M. Chandrashekhar, A. B. Greytak, ACS Appl. Electron. Mater. **3**, 1550 (2021).
[24] C. Gao, S. Sun, J. Liu, T. Shen, Y. Zhu, Funct. Mater. Lett. **14**, 2150017 (2021).
[25] U. Chalapathi, S. Sangaraju, Y. K. Kumar, R. Cheruku, P. Kondaiah, M. Lavanya, V. Gonuguntla, S. Alhammadi, M. D. Albaqami, M. Sheikh, S.-H. Park, Opt. Mater. **152**, 115492 (2024).
[26] U. Chalapathi, B. Poornaprakash, C.-H. Ahn, S.-H. Park, Ceramic. Int. **44**, 14844 (2018).
[27] U. Chalapathi, Y. K. Kumar, A. Sreedhar, V. Gonuguntla, N. H. Alotaibi, P. Rosaiah, S.-H. Park, J. Solid State Chem. **334**, 124691 (2024).
[28] B. D. Cullity, Elements of X-ray Diffraction, Addison Wesley, London, 1956.
[29] Satya N. Guin, Swastika Banerjee, Dirtha Sanyal, Swapan K. Pati, Kanishka Biswas, Inorg. Chem. **55**, 6323 (2016).
[30] Malik Dilshad Khan, Muhammad Aamir, Manzar Sohail, Sanket Bhoyate, Megan Hyatt, Ram K. Gupta, Muhammad Sher, Neerish Revaprasadu, Dalton Trans. **48**, 3714 (2019).
[31] Karen Trentelman, J. Raman Spectrosc. **40**, 585 (2009).
[32] Xiaoqi Fu, Tingshun Jiang, Qian Zhao, Hengbo Yin, J. Raman Spectrosc. **43**, 1191 (2012).
[33] U. Chalapathi, B. Poornaprakash, S.-H. Park, J. Power Source. **426**, 84 (2019).
[34] U. Chalapathi, A. S. Reddy, P. R. Prasad, G. Manjula, S. Sangaraju, R. Cheruku, B. A. Al-Asbahi, S. Alhammadi, C. P. Reddy, K. Mohanarangam, B. Purusottam Reddy, Si Hyun Park, Mater. Sci. Semicon. Proc. **168**, 107821 (2023).
[35] A. Nuñez Rodriguez, M. T. S. Nair, P. K. Nair, Mat. Res. Soc. Symp. Proc. **730**, 514 (2002).
[36] Y. Tabari-Saadi, Master's/PhD thesis). University of New South Wales, Sydney, Australia, 2022.

*Corresponding author: sihyun_park@ynu.ac.kr